Plasmon-Mediated Generation of Reactive Oxygen Species from Near-Infrared Light Excited Gold Nanocages for Photodynamic Therapy *in Vitro*

Liang Gao, Ru Liu, Fuping Gao, Yaling Wang, Xinglu Jiang, and Xueyun Gao*

CAS Key Laboratory for Biomedical Effects of Nanomaterials and Nanosafety, Institute of High Energy Physics, Chinese Academy of Sciences, Beijing 100049, China

ABSTRACT We have performed fundamental assays of gold nanocages (AuNCs) as intrinsic inorganic photosensitizers mediating generation of reactive oxygen species (ROS) by plasmon-enabled photochemistry under near-infrared (NIR) one/two-photon irradiation. We disclosed that NIR light excited hot electrons transform into either ROS or hyperthermia. Electron spin resonance spectroscopy was applied to demonstrate the production of three main radical species, namely, singlet oxygen ($^1O_2$), superoxide radical anion ($O_2^{-\bullet}$), and hydroxyl radical ($^\bullet OH$). The existence of hot electrons from irradiated AuNCs was confirmed by a well-designed photoelectrochemical experiment based on a three-electrode system. It could be speculated that surface plasmons excited in AuNCs first decay into hot electrons, and then the generated hot electrons sensitize oxygen to form ROS through energy and electron transfer modes. We also compared AuNCs' ROS generation efficiency in different surface chemical environments under one/two-photon irradiation and verified that, compared with one-photon irradiation, two-photon irradiation could bring about much more ROS. Furthermore, *in vitro*, under two-photon irradiation, ROS can trigger mitochondrial depolarization and caspase protein up-regulation to initiate tumor cell apoptosis. Meanwhile, hyperthermia mainly induces tumor cell necrosis. Our findings suggest that plasmon-mediated ROS and hyperthermia can be facilely regulated for optimized anticancer phototherapy.

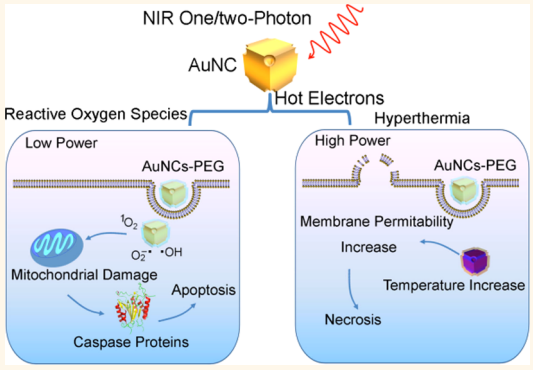

KEYWORDS: gold nanocages · reactive oxygen species · photodynamic therapy · plasmon-enabled photochemistry · hot electrons · two-photon

Reactive oxygen species (ROS), a number of free radicals derived from molecular oxygen, are produced as a consequence of energy or electron transport processes in photosynthesis.[1] High levels of ROS are reactive and potentially harmful to cells, causing oxidation of lipids, proteins, and DNA to trigger oxidative stress, and ROS have been utilized for tumor photodynamic therapy (PDT).[2] Conventionally, ROS originate from photoexcitation of organic photosensitizers (PSs) by converting their state from singlet state to triplet state, where photosensitization occurs through a type-I or -II photoprocess.[3] Recent years have witnessed a series of inorganic nanomaterials proved to be other mediators of ROS under irradiation, including typical semiconductor nanomaterials (quantum dots, TiO_2)[4,5] and carbon nanomaterials (fullerenes, nanotubes).[6−8] In particular, some pioneering studies corroborated that singlet oxygen ($^1O_2$), one kind of ROS, comes into being through energy transfer mode by direct irradiation of noble metal nanostructures with various morphologies using either continuous-wave (CW) or pulsed laser sources.[9−11] Great effort has also been paid to investigating the formation rule of $^1O_2$ and developing its therapeutic potential in the near-infrared (NIR) region, which is the ideal transparent window for PDT.[12,13] However, to the best of our knowledge, few reports introduced other kinds of ROS (superoxide radical anion ($O_2^{-\bullet}$) or hydroxyl radical ($^\bullet OH$)) generated *via* electron transfer mode under confined resonance conditions of noble metal nanostructures. Moreover, previous studies attempted to ascribe the origin of ROS to the photochemical reaction in

* Address correspondence to gaoxy@ihep.ac.cn.

Received for review April 29, 2014 and accepted July 3, 2014.

Published online July 03, 2014
10.1021/nn502325j

nanostructures' triplet excited state,[9,11] similar to the case of traditional organic PSs. Unlike the conventional opinion, currently, considerable attention has been focused on exploring the relationship between interfacial photochemical reaction and hot electron emission from noble metal nanostructures.[10] Unfortunately, there has been a lack of key data to confirm the hypothesis above. Also, few factors such as irradiation mode and interfacial environment have been found to influence the relaxation dynamics of optically excited hot electrons,[14,15] which were considered to further affect PDT efficiency. Therefore, prior to employing noble metal nanostructures as intrinsic PSs for PDT, it is imperative to expand the investigative scope of ROS, gain insights into the essence of ROS generation from the viewpoint of hot electron decay, and explore the essential factors influencing hot electrons' relaxation dynamics.

Meanwhile, since the photothermal therapeutic (PTT) capability of plasmonic metal nanostructures as the photothermal transducer has been extensively recognized,[16,17] the relevant mechanism of photoactivated tumor cell death has not yet been clearly understood. Few studies documented the mechanism above is involved with both hyperthermia and photosensitizing effects.[13,18] Very recently, Hwang *et al*. advocated that under NIR one-photon irradiation, by changing excitation wavelengths, gold nanorod-mediated phototherapeutic effects could be expediently varied from PTT to PDT.[13] The work gives a crucial indication that distinguishing and weighing the role of ROS and hyperthermia is vital to realize controlled individual or combined PDT and PTT. Nevertheless, most previous studies were carried out under NIR one-photon irradiation rather than two-photon irradiation. Although the latter irradiation mode requires expensive ultrafast pulsed lasers, it still provides a great opportunity to develop nonlinear optical effects of plasmonic metal nanostructures for advanced diagnose and phototherapy.

The original motivation of this article was a systematic investigation on plasmonic metal-mediated generation of ROS ($^1O_2$, $O_2^{-\bullet}$, and $^\bullet OH$) *via* energy and electron transfer modes under NIR one/two-photon irradiation for PDT, as shown in Scheme 1. Gold nanocages (AuNCs) were selected as representative plasmonic metal nanostructures due to their strong one/two-photon absorption in the NIR region. Moreover, the mechanistic insights of ROS damage of tumor cells internalizing PEGylated AuNCs as intrinsic inorganic PSs under two-photon irradiation were revealed in microscopic detail. Through adjusting the laser dosimetry, we elucidate that the extent of damage can be easily manipulated to fulfill the optimized phototherapy.

RESULTS AND DISCUSSION

AuNCs were prepared *via* a galvanic replacement reaction between Ag nanocubes and $HAuCl_4$ by following a procedure of Xia's group.[19] The transmission

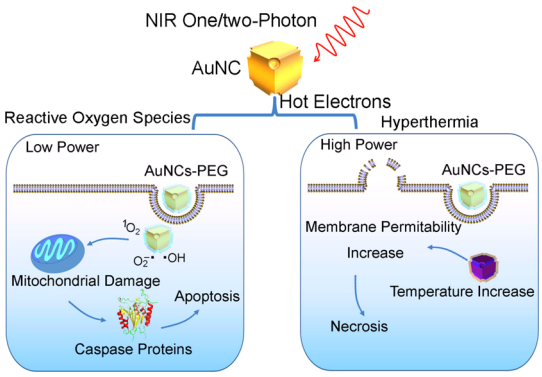

Scheme 1. Schematic illustration of AuNCs as intrinsic inorganic PSs mediating generation of ROS ($^1O_2$, $O_2^{-\bullet}$, and $^\bullet OH$) and hyperthermia under NIR one/two-photon irradiation. Depending on the irradiation power intensity, AuNC-PEG-mediated phototherapy could effectively affect tumor cells by two different pathways. ROS play a leading role in apoptosis at low power, and hyperthermia mainly results in necrosis at high power.

electron microscopy (TEM) image presents their typical morphology, with small holes at the corners and side faces (Figure 1a). The length of a single AuNC's outer edge is about 78 nm. The dynamic light scattering (DLS) size profile shows that the mean diameter of the nanoparticles is around 149 nm (Figure 1b), about two times the length of a single nanoparticle's outer edge, indicating that most AuNCs show limited aggregation in aqueous solution. Additionally, through inductively coupled plasma mass spectrometry (ICP-MS) analyses (see S1, Part I, SI), the constitution and concentration of AuNCs can be clarified to fulfill the following quantitative experimental requirements. Moreover, as displayed in Figure 1c, the surface plasmon resonance (SPR) peak of AuNCs is about 810 nm, to match the central wavelength of the one/two-photon NIR irradiation source. The molar extinction coefficient of AuNCs as prepared is approximately $1.7 \times 10^{10}\ M^{-1}\ cm^{-1}$ at 810 nm based on the Lambert–Beer law (see S1, Part II, SI), which is about 5 orders of magnitude higher than that of conventional organic PSs. The strong absorption of AuNCs in the NIR transparent window enables them to be potential intrinsic inorganic PSs for PDT. It should be mentioned that our experimentally measured extinction coefficient of aggregated AuNCs is very close to that of the theoretically calculated monodispersed AuNCs (see S1, Part II, SI). The result implies that the limited aggregation above scarcely induces deviation of the extinction coefficient and further ROS production efficiency.

Evidence of oxygen-centered radicals is crucial to interpret metal nanostructures' plasmon-enabled photochemistry. Electron spin resonance (ESR) spectroscopy was applied to verify the generation of three main radical species, namely, $^1O_2$, $O_2^{-\bullet}$, and $^\bullet OH$. 2,2,6,6-Tetramethyl-4-piperidone (TEMP, for $^1O_2$) and 5,5-dimethyl-1-pyrroline *n*-oxide (DMPO, for $O_2^{-\bullet}$ and $^\bullet OH$) were exploited as ROS-sensitive trapping agents[6] to disclose ROS production from AuNC dispersion

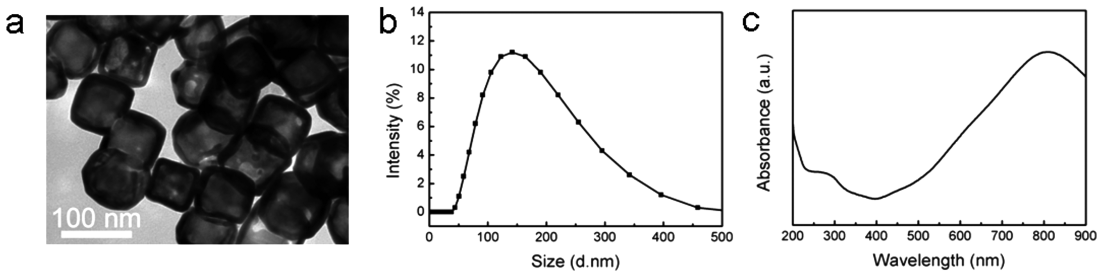

Figure 1. (a) TEM image, (b) DLS size profile, and (c) UV−vis spectrum of AuNCs.

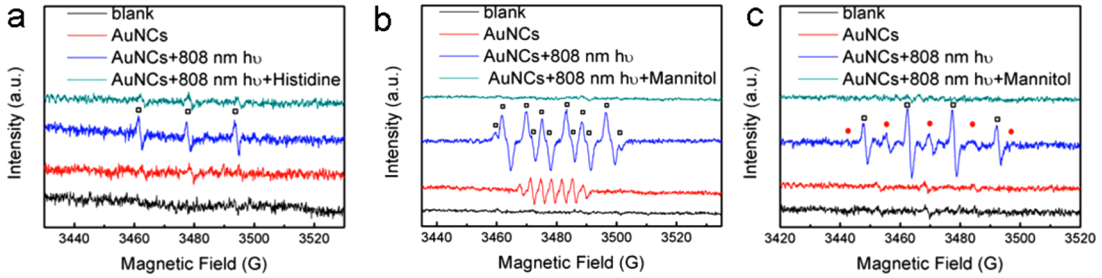

Figure 2. ESR spectra of three main ROS spin adducts generated by 0.9 nM AuNCs under irradiation by an 808 nm CW light with mean power intensity at 4.3 W cm^{-2} for 3 min (blue curve). Control experiments without light or AuNCs (black curve); in which light is omitted (red curve), and in the presence of ROS scavenger, 10 mM histidine or 10 mM mannitol (green curve). (a) $^1O_2$: TEMP-$^1O_2$ adduct in aqueous solution containing 0.3 M TEMP; (b) $O_2^{-\bullet}$: DMPO-OOH adduct in DMSO containing 0.2 M DMPO; (c) $^\bullet$OH: DMPO-OH adduct in aqueous solution containing 0.1 M DMPO.

under ~810 nm one-photon light irradiation. As shown as blue curves in Figure 2a, the ESR signal for irradiated O_2-saturated AuNC dispersion clearly displays a characteristic 1:1:1 triplet line with a hyperfine splitting constant (a_N = 16.3 G), which is the feature of a TEMP-$^1O_2$ (TEMPO) spin adduct. In contrast, under similar conditions, in the absence of AuNCs and light, TEMPO formation does not occur (Figure 2a, black curve). However, it is interesting to find that weaker characteristic peaks appear in AuNC dispersion without light irradiation (Figure 2a, red curve), which might be ascribed to oxygen activation during the chemisorption on a metal surface, in agreement with the previous report.[20] To provide further evidence to support the involvement of $^1O_2$ in the photosensitization process, histidine as a specific $^1O_2$ scavenger[6] was employed. It can be seen that the intensity of the ESR signal decreases markedly (Figure 2a, green curve). Likewise, the formation of $O_2^{-\bullet}$ is clarified by the ESR spectrum, consisting of two components (a_N = 14.2 G, a_H^β = 11.4 G, $a_H^{\gamma 1}$ = 1.3 G, Figure 2b, blue curve), which is indicative of a DMPO-OOH adduct. It should be noted that the reaction is carried out in dimethyl sulfoxide (DMSO) in order to quench $^\bullet$OH generated under the reaction conditions because $^\bullet$OH could react rapidly with DMPO, thus disturbing the spectrum of DMPO-OOH.[6] What is more, the lifetime of $O_2^{-\bullet}$ in DMSO is much longer than that in H_2O, which means that $O_2^{-\bullet}$ can be much more easily spin trapped in DMSO. The inhibition effect is so obvious by adding mannitol, a quencher for $O_2^{-\bullet}$,[7] that no ESR signal is detected (Figure 2b, green curve). The signal of DMPO-OOH is undetected in the AuNC aqueous suspension under irradiation (data not shown). It could be explained that the generated $O_2^{-\bullet}$ could undergo rapid dismutation to form other ROS (H_2O_2 and $^\bullet$OH) in aqueous solution.[8,21] As expected, the illumination of a AuNC and DMPO aqueous suspension leads to formation of a large amount of DMPO-OH spin adducts, which can be easily distinguished by a typical four-line spectrum (Figure 2c, blue curve, black hollow squares) with a relative intensity ratio of 1:2:2:1 and equivalent hyperfine splitting constants (a_N =14.9 G, a_H = 14.9 G). It should be mentioned that $^\bullet$OH is a highly active radical, and once it is generated, adjacent carbon-centered organic compounds could be attacked. The as-obtained carbon-centered radicals could be subsequently spin trapped by DMPO (Figure 2c, blue curve, red solid circles).[21,22] $^\bullet$OH generation is further confirmed by introducing mannitol ($^\bullet$OH quencher).[7] In this case, the signal has almost vanished (Figure 2c, green curve).

Experimental observations of photoinduced AuNC-assisted ROS generation could be accounted for by hot electron related photoreactions taking place *via* energy and electron transfer modes. The existence of hot electrons from irradiated AuNCs is illustrated by a well-devised three-electrode system. Relevant photoelectrochemical experiments were operated on an electrochemical workstation.[23] A saturated calomel electrode (SCE) and Pt rod were employed as the reference electrode and counter electrode, respectively. The generated photocurrents were measured between the AuNC-modified indium tin oxide (ITO) working electrode and counter electrode under

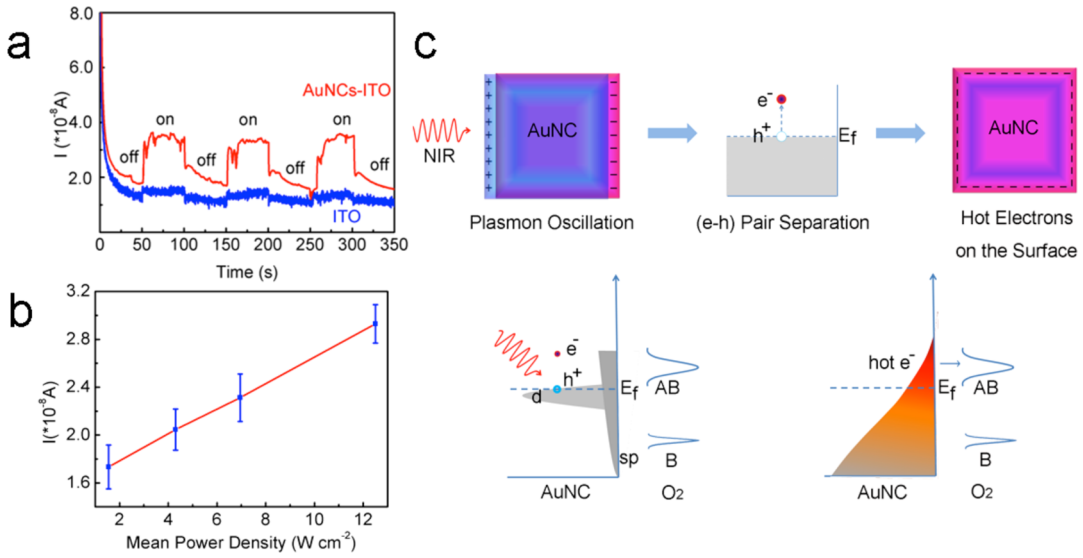

Figure 3. (a) Photocurrent responses of the AuNC-modified ITO (red curve) or bare ITO (blue curve) electrode to repetitive illumination and darkness cycles, respectively. The mean power density is 12.5 W cm^{-2}, and the initial potential is E = 0.25 V *versus* SCE. (b) Photocurrent responses of the AuNC-modified ITO electrode to illumination with different mean power densities. The initial potential is E = 0.25 V *versus* SCE. (c) Surface plasmon resonance generated from NIR light irradiated AuNCs and hot electron production from plasmon decay. The hot electrons with high energy have sufficient energy to transfer into and populate the antibonding (AB) O−O orbital.

illumination at different mean power densities. Figure 3a presents the much more evident switchable generation of the photocurrent responding to a cyclic "on−off" illumination of the AuNC-modified ITO electrode, compared with that in the case of an unmodified ITO electrode. Obviously, the intensity of the photogenerated current can be varied by adjusting the mean power density of light implemented to illuminate the photoanode above (Figure 3b). On the basis of the fact that photogenerated hot electron emission accompanying ROS generation is explicit as discussed above, the mechanism of photochemistry could be speculated as follows, displayed in Figure 3c. In detail, surface plasmons excited in AuNCs first decay into hot electrons with energies between vacuum level and Fermi level of the metal. Hot electrons in the high-energy tail will further extend away from the AuNCs rather than keep an equilibrium electron distribution and transfer into and populate the $2\pi^*$ antibonding (AB) O−O orbital, creating a transient negative ion, $O_2^{-\bullet}$. Then $O_2^{-\bullet}$ relaxes by releasing an electron back to the AuNCs surface.[24,25] When the electron back-transfer process leads to a spin-flip process in O_2, changing its electron spin state, $^1O_2$ could come into being. Meanwhile, $^\bullet$OH could stem from the photogenerated $O_2^{-\bullet}$ by following a series of reactions:[8]

$$O_2^{-\bullet} + 2H^+ + e^- \rightarrow H_2O_2 \quad (1)$$

$$H_2O_2 + H^+ + e^- \rightarrow {}^\bullet OH + H_2O \quad (2)$$

In order to estimate the conversion efficiency from light energy to chemical energy, quantitative evaluations of ROS yields of photochemical reaction were conducted. Since $O_2^{-\bullet}$ in aqueous solution is unstable as verified by ESR and its quantitative detection becomes difficult, we thus focus on the yields of $^1O_2$ and $^\bullet$OH under one/two-photon irradiation. First, $^1O_2$ quantum yield measurement was carried out using singlet oxygen sensor green (SOSG, a specific fluorescence probe) by following a reported protocol.[26] The CW diode laser and femtosecond Ti:sapphire laser tuned to ~810 nm at a mean power density of about 23 mW cm^{-2} were selected as one/two-photon irradiation sources, respectively. Indocyanine green (ICG), with an identified one-photon sensitization quantum yield at a 780 nm absorption peak,[27] was chosen as the reference. Quantification of $^1O_2$ quantum yield of AuNCs is estimated by comparing the photosensitizing reaction rate of AuNCs with that of ICG (shown in Figure 4a, b, and c). The detailed method and calculation process are described in S1, Part III, SI. As a consequence, AuNCs' $^1O_2$ quantum yield is found to be 0.006 and 0.04 under CW and pulsed laser irradiation, respectively, disclosing an astonishing 6-fold increase of $^1O_2$ production capability under two-photon irradiation from that under one-photon conditions. The remarkable distinction in $^1O_2$ production under two different irradiation modes can be well justified on the grounds of heat generation.[10] The heating mechanism of AuNCs excited by a pulsed laser could be entirely different from that irradiated by a CW laser which encounters rapid conductive/convective heat loss to the surrounding water. According to the pioneering study of ultrafast laser spectroscopy by Xia's group,[28] the electrons of AuNCs can be excited by a pulsed laser to become hot electrons on a picosecond time scale. Subsequently, hot electrons equilibrate

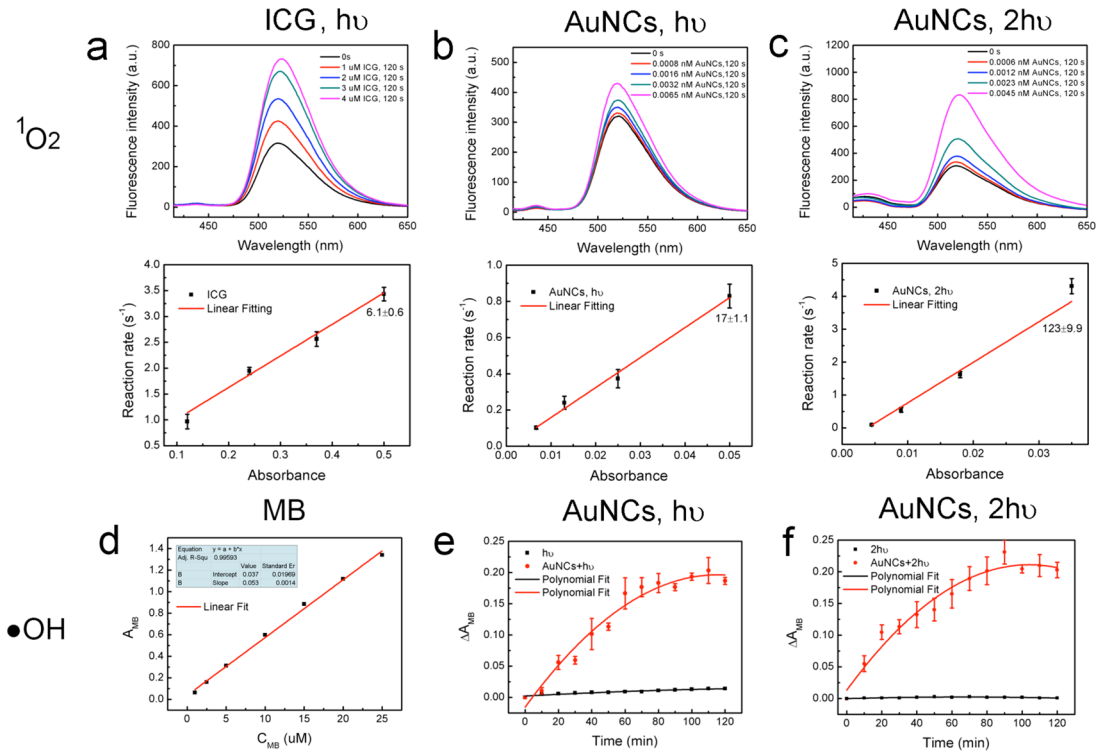

Figure 4. Quantitative measurements of $^1O_2$ and •OH generation by using SOSG and MB as the reporter probes. Fluorescence enhancement of SOSG accompanying reaction of 6.0 μM SOSG with $^1O_2$ generated from ICG or AuNCs at different concentrations. (a) ICG under NIR one-photon irradiation; AuNCs under NIR (b) one- or (c) two-photon irradiation at 23 mW cm^{-2} for 120 s (upper), and the relevant reaction rates as a function of ICG or AuNC absorbance (lower). (d) Concentration-dependent absorbance intensity of MB at 664 nm. Discoloration of MB (ΔA_{MB}) in the presence (red curve) or absence (black curve) of AuNCs as a function of irradiation time under NIR (e) one- or (f) two-photon irradiation.

with the lattice through an electron−phonon coupling process and transfer the energy to the surroundings on a time scale of 10−100 ps. In other words, the laser pulse width (100 fs) is shorter than the hot electrons' relaxation time with the lattice (10−100 ps), which can initiate extreme heat confinement, leading to a rapid temperature increase. It can be speculated that higher temperatures raise the $^1O_2$ quantum yield in at least two pathways. On one hand, a higher temperature means a higher hot electron yield,[29] thus suggesting higher $^1O_2$ production *via* the energy transfer mode as discussed above. On the other hand, direct conversion of O_2 to $^1O_2$ by a thermal pathway should not be neglected.[10,30] Notwithstanding the $^1O_2$ quantum yield is somewhat low, considering AuNCs' much higher NIR absorption cross section[31] as well as good resistance to photobleaching and enzymatic degradation, AuNCs are superior to traditional organic PSs in PDT.

To our best knowledge, AuNCs' •OH quantum yield cannot be determined by the similar method above owing to the lack of referenced PS with identified sensitization quantum yield. We merely compared its absolute generation under one/two-photon irradiation by a reported methylene blue (MB) photobleaching method.[32] MB is specific to examine •OH, and neither $^1O_2$ nor $O_2^{-\bullet}$ causes its photobleaching.[32] The amount of produced •OH was qualitatively evaluated by monitoring the discoloration of MB (ΔA_{MB}) through colorimetry. As presented in Figure 4e and f, the black curves reveal that MB can be only slightly degraded under NIR light irradiation without AuNCs, implying that under this condition, MB is a stable molecule and the photolysis can be ignored. In contrast, the red curves indicate that the generated •OH mediated by AuNCs is first directly proportional to the irradiation time and then levels off after 90 min under one/two-photon irradiation. It is somewhat surprising, distinct from AuNCs' 6-fold increase of $^1O_2$ production capability under two-photon irradiation from that under one-photon condition, that •OH generation under two irradiation modes is almost identical (3.8 and 4.0 μM, respectively). The detailed calculation process is given in S1, Part IV, SI. Although the reason is not clearly understood currently and warrants further study, a possible explanation could be that $^1O_2$ generation is through an energy transfer process, whereas •OH is derived from an electron transfer process.

In brief, the results above indicate two-photon irradiation is the preferred irradiation mode to obtain much higher ROS generation efficacy. In addition, two-photon excitation is highly localized, which might be advantageous over one-photon excitation in treating sensitive tissues.[33] Last but not at least, two-photon excitation can simultaneously realize NIR PDT and

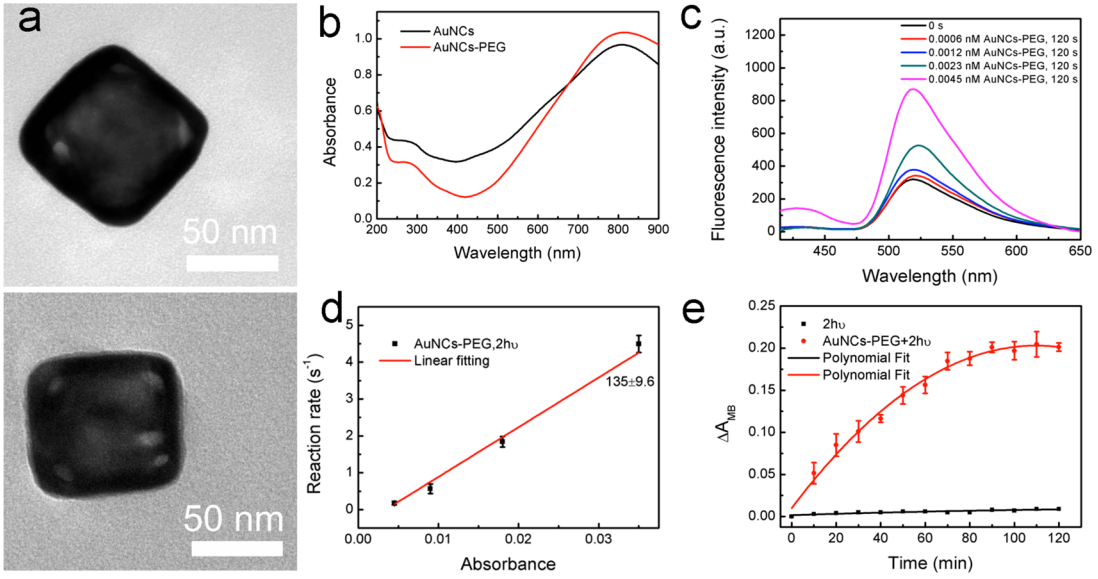

Figure 5. (a) TEM images of a single AuNC before (upper) and after (lower) PEGylation. (b) UV−vis spectra of AuNCs and AuNCs-PEG in H_2O. (c) Under two-photon irradiation at 23 mW cm^{-2} for 120 s, fluorescence enhancement of SOSG accompanying reaction of 6.0 μM SOSG with $^1O_2$ generation from AuNCs-PEG at different concentrations. (d) Relevant reaction rate as a function of AuNCs-PEG absorbance. (e) Time-dependent discoloration of MB (ΔA_{MB}) in the presence (red curve) or absence (black curve) of AuNCs-PEG under NIR two-photon irradiation at 23 mW cm^{-2}.

bioimaging, which is superior to one-photon irradiation in the tumor theranostic field.[33] We thereupon concentrate on exploring the role of therapeutic ROS in cell damage under two-photon irradiation.

To improve the biological compatibility of AuNCs and examine the effect of ligand function on plasmon-enabled photochemistry, surface modification of AuNCs with a monolayer of methoxy-terminated poly(ethylene glycol) thiol (HS-PEG_{5000}-OMe) was conducted. The explicit distinction of AuNCs before and after PEGylation in morphology (Figure 5a) and plasmon resonance (Figure 5b) can be ascribed to the conversion of the surface coating of AuNCs from poly(vinylpyrrolidone) (PVP) to HS-PEG_{5000}-OMe. The results of the size profile and stability test of AuNCs-PEG are presented in Figure S1a and S1b (S3, SI). The obtained nanoparticles are generally stable in H_2O, PBS, and Dulbecco's modified Eagle medium (DMEM) cellular medium because there is no noticeable aggregation within 2 weeks, as shown in Figure S1c (S3, SI). $^1O_2$ and $^{\bullet}OH$ production by PEGylated AuNCs (Figure 5c, d, and e) are subsequently observed to occur at similar rates as that in the case of PVP-coated AuNCs under two-photon irradiation. The results reveal that the change of the surface chemical environment has no marked impact on ROS generation. This could be due to the similarity in the lifetime and dynamics of hot electrons before and after ligand exchange.[15]

After determination of the optimized dosage and exposure time (0.025 nM, 24 h), the number of AuNCs-PEG per cell (232 ± 23), and the location (lysosome) of AuNCs-PEG for model tumor cells *in vitro* (see S2, Parts I, II, III, and S3, Figure S2 in the SI), we assessed the level of ROS inflicted by photoactivated AuNCs-PEG using 5-(and-6)-chloromethyl-2′,7′-dichlorodihydrofluorescein diacetate acetyl ester (CM-H_2DCFDA), a specific ROS dye. Assessment of intracellular ROS level was realized by analyzing the mean fluorescence intensity. It is noteworthy that cell damage can be adjusted by a series of parameters.[34] In order to simplify the experimental process, two factors (dosage and irradiation time) were kept constant and tumorigenic cell damage was tested as a function of irradiation power. After continuous scanning with a ~810 nm fs-pulsed laser at two typical power intensities for 300 s, ROS generation in HeLa cells pretreated with AuNCs-PEG was monitored *in situ*. At high illumination power (14 pJ per pulse), fluorescence is distributed in the whole cells (Figure 6aA), including the nucleus and cytoplasm, a sign of overwhelming oxidative stress. To further confirm ROS production, under the same power, cells treated with AuNCs-PEG and ROS quenchers (histidine and mannitol) were irradiated. In this case, green fluorescence has almost vanished (Figure 6aB), implying ROS generation is completely inhibited by ROS quenchers. By decreasing the power to 0.40 pJ per pulse, the ROS level significantly decreased as expected (Figure 6aC). Comparatively, there is no detectable ROS in a series of control cells (Figure 6aD, E, and F). It should be emphasized that, to quantitatively analyze the generated ROS, all the fluorescent images were collected at the same setting, and the corresponding mean fluorescence intensities are quantitatively analyzed in Figure 6b.

With the aim of visualizing cell injury through either a necrotic or apoptotic pathway and illuminating the relevant mechanism, phototoxicity induced by

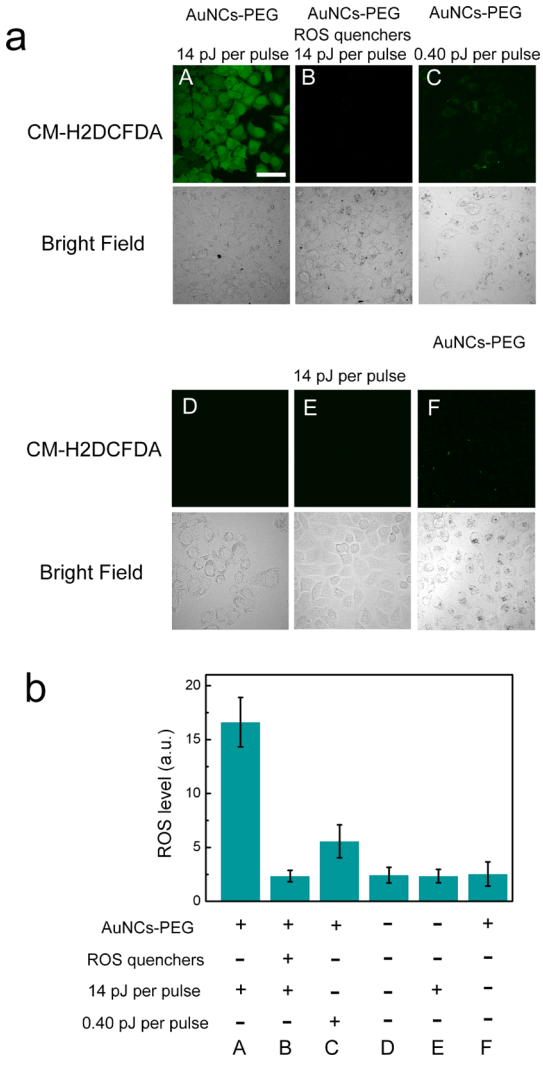

Figure 6. Two-photon laser illumination of AuNCs-PEG-treated HeLa cells causes oxidative stress detected by ROS probe CM-H_2DCFDA, which emits green fluorescence when oxidized by ROS. (a) CLSM images of HeLa cells under different conditions. Cells that were incubated in the presence of AuNCs-PEG under illumination at 14 (A) and 0.40 (C) pJ per pulse; (B) with AuNCs-PEG, in the presence of ROS quenchers (250 μM histidine and 250 μM mannitol) under irradiation at 14 pJ per pulse; (D) devoid of AuNCs-PEG or irradiation; (E) receiving light irradiation at 14 pJ per pulse; (F) receiving AuNCs-PEG without irradiation. The irradiation time is set to 300 s. Scale bar is 50 μm. (b) Quantitative comparison of ROS generation in corresponding panels A−F. Data are shown as mean ± the standard error from more than 20 independent cells.

irradiation of cells enveloped with AuNCs-PEG was explored by a standard FITC-annexin V/propidium iodide (PI) double staining assay. To quantitatively analyze cell death under high/low irradiation power as mentioned above, the percentages of necrotic, apoptotic, and dead cells were determined by dividing the number of labeled cells with the total number of cells (>30 cells) counted in three individual images. At high power, 88(±8)% of AuNCs-PEG-pretreated cells undergo necrosis, with both membranes (green) and nuclei (red) stained (Figure 7aA and bA). The damage could arise from the drastic cavitation formed during the process of irradiation (see blue and green arrows in Figure S3a), which was proposed to cause a temporary rupture of the cell membrane and increase membrane permeability.[35] Even if adequate ROS quenchers were delivered, no obvious cell viability (73(±5)% necrotic cells) is recovered (Figure 7aB and bB). Noticing that ROS quenchers can reverse oxidant stress as mentioned above (Figure 6aB and bB), it is safe to draw the conclusion that at high irradiation power (14 pJ per pulse) thermal disruption of plasma membrane integrity provides the most direct opportunity to trigger necrosis, compared with that of ROS effects. What is more, the ultimate temperature of AuNCs-PEG-endocytosed single HeLa cells upon high power irradiation is roughly estimated to be about 54 °C (see S2, Part V, SI). This result is in good accordance with the previous report that temperatures higher than 50 °C could evoke irreversible cell damage and necrosis.[36] At low power (0.40 pJ per pulse), 25(±4)% of irradiated cells display apoptotic characteristics (Figure 7aC and bC). On the basis of the facts that no detectable photothermal effect is observed (Figure S3b) and the estimated temperature of the single cell after irradiation is around 28 °C (see S2, Part V, SI), hyperthermia-induced apoptosis as the underlying mechanism can be excluded. As expected, the apoptotic behaviors are evidently compromised by introducing ROS quenchers, with significantly decreased fluorescence intensity on the plasma membranes (Figure 7aD and bD, 6(±2)% apoptotic cells). The results above allow us to deduce that AuNC-sensitized ROS play a leading role in triggering the apoptotic pathway at low illumination power. As a comparison, the negative control cells do not show any significant necrotic or apoptotic features (Figure 7aE and bE). Furthermore, the necrotic cells with instant thermal disruption of the plasma membrane make up *ca.* 73(±5)% of the irradiated cells, while the cells with apoptotic characteristics after exposed to ROS merely account for 25(±4)%. Obviously, it seems that PTT is more effective in instantly killing the cells than PDT. However, considering that apoptosis promoted by PDT is a programmed process that involves time-consuming complex signaling pathways,[37] it is necessary to carry out relevant time-dependent experiments to re-evaluate the efficiency of PDT. As shown in Figure S5a, 24 h after irradiation at low power, it is evident that most cells show a brighter green fluorescence staining than that obtained from cells by instant staining (Figure 7aC). Some cells even show late apoptotic characteristics, with both membrane and nuclear staining. As expected, 48 h after irradiation, the features of late apoptosis are much more obvious than those obtained at 24 h, as shown in Figure S5b. The results demonstrate that compared with PTT as an ablation strategy related to acute and accidental necrosis, apoptosis promoted by PDT is

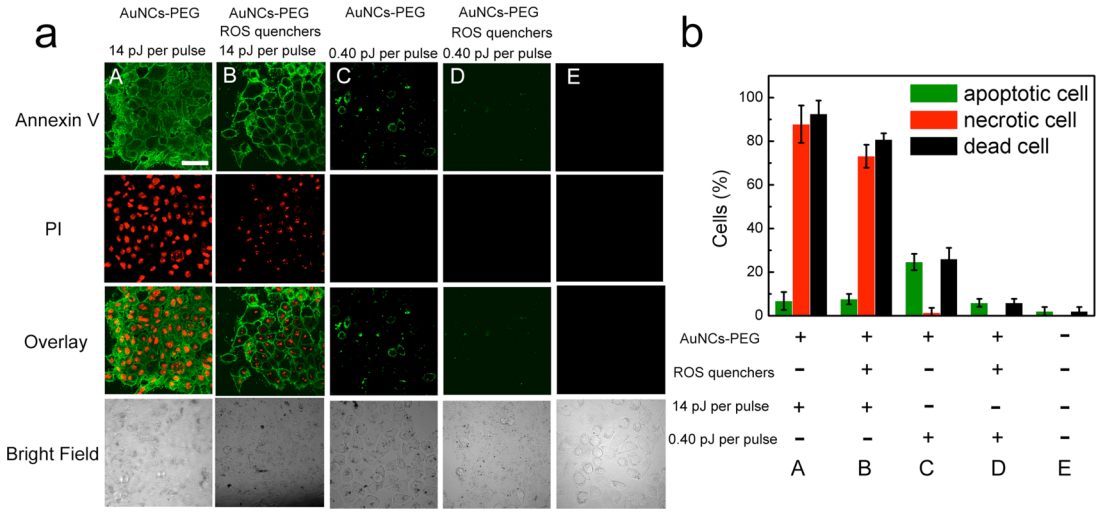

Figure 7. (a) CLSM images of controlled apoptosis and necrosis of HeLa cells under different conditions. Cells incubated in the presence of AuNCs-PEG under two-photon irradiation at (A) 14 and (C) 0.40 pJ per pulse; with AuNCs-PEG and ROS quenchers (250 μM histidine and 250 μM mannitol) under irradiation at (B) 14 and (D) 0.40 pJ per pulse; (E) devoid of AuNCs-PEG or irradiation as control groups. The irradiation time is set to 300 s. After irradiation, cells were stained with FITC-annexin V (green) and PI (red) to monitor apoptotic and necrotic cells, respectively. Scale bar is 50 μm. (b) Percentage of apoptotic, necrotic, and dead cells corresponding to panels A−E. Data are shown as mean ± standard error from three independent images.

considered to be a programmed and controlled therapeutic modality, which can be used to overcome the limitations of PTT.

To further inquire into the mechanism of AuNC-generated ROS initiating cell apoptosis, an investigation of subcellular organelle rupture and biochemical changes of photodamaged cells at low irradiation power was conducted. At the molecular level there are two principle mechanisms for apoptotic cell death, that is, the extrinsic death-receptor pathway and the intrinsic mitochondrial pathway.[37] Since mitochondrial vulnerability to oxidants is emphasized by their limited ability to cope with ROS, the latter pathway may be more suitable for explaining the apoptosis mechanism in our present study. Herein, the commercial fluorescent dye 5,5′,6,6′-tetrachloro-1,1′,3,3′-tetraethylbenzimidazolocarbocyanine iodide (JC-1) was employed to conveniently validate mitochondrial depolarization induced by ROS.[38] As depicted in Figure 8a and c, mitochondria depolarization is indicated by a decrease in the red (JC-1 aggregate)/green (JC-1 monomer) fluorescence intensity ratio when excited by a 488 nm laser. On the contrary, for cells treated with ROS quenchers, less mitochondria damage is observed, which can be reflected by the increase of red fluorescence intensity (Figure 8b). If mitochondrial damage is very serious, a cascade process is initiated. At this moment, many biomolecules will be released from the mitochondria into the cytosol and form a complex to activate a specific series of cytoplasmic proteases, termed caspases, which will activate caspase-3/7 and other downstream caspases to induce apoptosis terminally.[37] The activity of caspase-3/7, one crucial caspase protein, was monitored by using caspase protein activated dye NucView 488 caspase-3/7

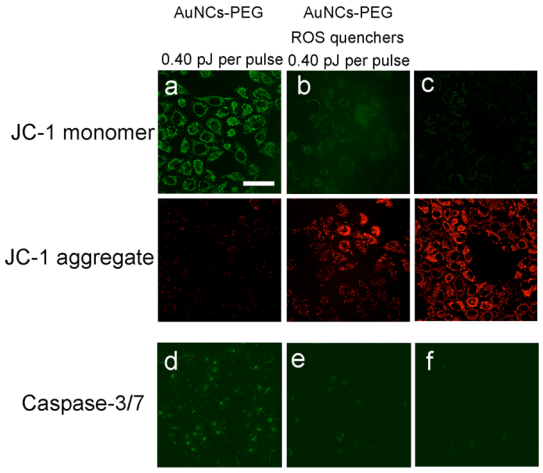

Figure 8. CLSM images of mitochondrial membrane potential (JC-1 staining) of cells pretreated with AuNCs-PEG in the absence (a) or presence (b) of 250 μM ROS quenchers under NIR two-photon irradiation at 0.40 pJ per pulse; (c) control cells. CLSM images of caspase-3/7 activity of cells pretreated with AuNCs-PEG in the absence (d) or presence (e) of 250 μM ROS quenchers under NIR two-photon irradiation at 0.40 pJ per pulse; (f) control cells. Scale bar is 50 μm.

substrate[39] to stain the nucleus with bright green fluorescence (Figure 8d). As a comparison, for cells treated with ROS quenchers, less caspase-3/7 is expressed, which is indicated by the relatively dimmer green fluorescence in the cell nucleus (Figure 8e). One can see a similar result in the control group (Figure 8f). All the results above lend support to AuNCs-mediated ROS causing tumor cell apoptosis by the intrinsic mitochondrial pathway where mitochondrial failure and apoptosis-involved caspase protein expression occur.[37]

It is widely known that necrosis is featured by failure of plasma membrane and release of cellular contents, causing adverse inflammatory reaction. In contrast,

in early apoptotic cells, leakage of cellular contents into surrounding tissues can be prevented, enabling apoptosis as a clean cell death process that minimizes the risk of inflammation.[40] In the present study, by tuning down laser power intensity, apoptosis induced by AuNC-mediated ROS under two-photon irradiation could be easily regulated to be a mild process. In cancer treatment, it can be anticipated to alleviate strong adverse inflammatory responses[41] to surrounding normal tissues and diminish unfavorable sequelae effects[42] causing the subsequent growth of distant metastatic tumors.

CONCLUSIONS

In conclusion, detailed exploratory experiments were carried out to disclose ROS ($^1O_2$, $O_2^{-\bullet}$, and $^\bullet OH$) generation from NIR light excited AuNCs as intrinsic PSs. We preliminarily presume that ROS are generated *via* plasmon-produced hot electrons through energy and electron transfer modes. Besides, the efficacy of $^1O_2$ generated by AuNCs exhibits a 6-fold increase under femtosecond-pulsed excitation conditions, compared with that under CW excitation conditions, whereas $^\bullet OH$ yield is not affected by the identical law. AuNCs-PEG-mediated production of ROS under two-photon irradiation represents a preferred approach for inducing clean tumor cells death, complementary to hyperthermia. One may speculate that simply adjusting the laser power to initiate cell apoptosis as an optically controlled injury is anticipated to break through the inherent limitation of individual PTT. The present strategy could be a good reference for employing other biocompatible noble metal nanomaterials as PSs for PDT.

METHODS SECTION

Chemicals and Reagents. $AgNO_3$, $Na_2S\cdot 9H_2O$, $HAuCl_4\cdot 3H_2O$, ethylene glycol (EG), acetone, anhydrous chloroform, DMSO, and ethanol were purchased from Beijing Chemical Reagent Co., China. TEMP, DMPO, and PVP with average $M_r \approx 55\,000$ were from Sigma-Aldrich. Deuterium oxide (D_2O, 99.9%) was obtained from Cambridge Isotope Laboratories, USA. SOSG, Lysotracker, Hoechest 33342, and CM-H_2DCFDA were bought from Molecular Probes, USA. NucView 488 caspase-3/7 substrate was from Biotium, USA. ICG was purchased from TCI, Japan. D-Mannitol, L-histidine, and MB were from Amresco, USA. SH-PEG_{5000}-OMe was obtained from JenKem Technology Co., Ltd., China. FITC-annexin V/PI kit and JC-1 were bought from Beyotime Institute of Biotechnology, China. Cell culture medium DMEM and fetal bovine serum (FBS) were purchased from Hyclone. Cell counting kit-8 (CCK-8) reagent was from Dojindo Laboratories, Japan. All other materials were commercially available and used as received unless otherwise mentioned. The water, with a resistivity of 18.2 MΩ·cm, used throughout the experiment, was purified with a Milli-Q system from Millipore Co., USA.

Fabrication of AuNCs and AuNCs-PEG. AuNCs were prepared by a galvanic replacement reaction between Ag nanocubes serving as the sacrificial templates and $HAuCl_4\cdot 3H_2O$ by following a method reported by Xia's group.[19] Then AuNCs were derivatized with SH-PEG_{5000}-OMe. Briefly, 5 mg of SH-PEG_{5000}-OMe was dissolved in 10 mL of H_2O in a vitreous vial, followed by adding 1 mL of AuNCs at a final concentration of 1.5 nM. The reaction aqueous solution was stirred for 12 h. The excess SH-PEG_{5000}-OMe was removed by centrifugation at 10 000 rpm for 20 min, and the obtained AuNCs-PEG were then washed with H_2O for several times and resuspended in H_2O or PBS for further use.

Characterization. The morphologies of the AuNCs and AuNCs-PEG were examined by a JEOL 2011 transmission electronic microscope working at 200 kV. The average size analysis was performed with Image software (ImageJ 1.43) by manually measuring the AuNC's outer and inner edge length for at least 20 nanocages. All absorption spectra were obtained using a UV-1800 UV−visible spectrometer (Shimadzu, Japan). The mean diameter and size distribution of AuNCs and AuNCs-PEG were documented by a phase analysis light scattering technique (Zetasizer Nano, Malvern). All fluorescence measurements were performed on an RF-5301PC fluorescence spectrometer equipped with a Xe arc lamp (Shimadzu, Japan). Excitation and emission slits were set to 10 nm. The ESR spectra were measured by using a Bruker model ESP 300 spectrometer operating at room temperature. Au and Ag contents were determined by ICP-MS (Thermo Elemental X7, USA). A CW laser at 808 nm was used as the NIR one-photon excitation source (BWT Beijing LTD, China). One-photon fluorescence and two-photon luminescence images were obtained by a two-photon laser scanning microscope (Olympus, attached to a Nikon fluoview multiphoton microscope (FV1000MPE)). A mode-locked femtosecond Ti:sapphire laser tuned to 810 nm with a repetition rate of 80 MHz and pulse width of 100 fs was used as the two-photon illumination source.

ICP-MS Analysis of AuNCs. A 25 μL amount of the prepared AuNCs was digested by 20 mL of *aqua regia* in a 50 mL beaker at mild boiling temperature. The solution was evaporated to 1−2 mL and cooled at room temperature before diluted by 2% HNO_3 and 1% HCl to a final 50 mL volume. Calibration plots for standard Au were obtained by injecting a series of standard aqueous Au solutions (0.1, 0.5, 1, 5, 10, 50, 100 ng mL^{-1} containing 2% HNO_3 and 1% HCl) into the ICP-MS system, followed by the completely digested AuNC solution. Bismuth and indium (each 20 ng mL^{-1}) were regarded as an internal standard, respectively. Each experiment was performed in triplicate. Quantification was performed by external seven-point calibration, by which the atomic percentages and the concentration of AuNCs were determined by calculations.

ESR Measurements. *$^1O_2$.* To 100 μL of a 1.3 nM AuNC D_2O suspension was added 40 μL of 1.0 M TEMP D_2O aqueous solution, and the resulting solution was mixed well. The sample was then injected into quartz capillaries designed specifically for ESR analysis and subjected to high-purity oxygen for 3 min. The mixture was irradiated with 808 nm CW light at 4.3 W cm^{-2} for 3 min and immediately subjected to ESR measurement. Parameter settings: microwave power, 10.12 mW; frequency, 9.8 GHz; time constant, 40.96 ms; scan width, 100 G. ESR signals of the TEMP-$^1O_2$ adduct generated in the presence of TEMP without irradiation; TEMP and AuNCs without irradiation; and TEMP, AuNCs, and 10 mM histidine, a $^1O_2$ scavenger, with irradiation were collected as control groups.

$O_2^{-\bullet}$. To 50 μL of a 1.1 nM AuNC DMSO suspension was added 10 μL of 1.0 M DMPO in DMSO, and the resulting solution was mixed well. The mixture was irradiated by a 808 nm CW light at 4.3 W cm^{-2} for 3 min and immediately subjected to ESR measurement. Parameter settings were the same as described above. ESR signals of DMPO-OOH generated in the presence of DMPO without irradiation; DMPO and AuNCs without irradiation; and DMPO, AuNCs, and 10 mM mannitol, an $O_2^{-\bullet}$ scavenger, with irradiation were collected as control groups.

$^\bullet OH$. To 100 μL of a 1.0 nM AuNC suspension in H_2O was added 15 μL of a 1.0 M DMPO aqueous solution, and the resulting solution was mixed well. The following procedure was the same as the $O_2^{-\bullet}$ detection assay. The ESR signals of DMPO-OH generated in the presence of DMPO without irradiation; DMPO and AuNCs without irradiation; and DMPO, AuNCs,

and 10 mM mannitol, a •OH scavenger, with irradiation were collected as control groups.

Photocurrent Measurements. Electrochemical measurements were recorded on an electrochemical workstation (CHI600E, Shanghai Chenhua Instrument Co. Ltd., China) at 16 °C under air. The SCE and Pt rod (d = 0.5 mm, l = 6 cm) were used as the reference electrode and counter electrode, respectively. A buffer solution containing 50 mM KCl, 15 mM $CaCl_2$, 15 mM $MgCl_2$, and 40 mM 2-morpholinoethanesulfonic acid (MES) was employed as an electrolyte solution at pH 6.4. Then 100 μL of 0.15 nM AuNCs was dropped onto a piece of tailored ITO glass (1 cm × 2 cm) and dried under vacuum at room temperature to form a AuNC-modified ITO electrode. The final covered area was about 1.2 cm^2. Photocurrent measurements were performed using a homemade system including the adjustable CW laser (λ = 808 nm) mentioned above. The generated photocurrents were measured between the bare ITO or AuNC-modified ITO (about 1 cm^2) working electrode and the counter electrode under illumination at different mean power densities. The effective illuminated area was about 0.20 cm^2. The initial potential was set at E = 0.25 V.

Quantitative Measurement of $^1O_2$ Quantum Yield. In $^1O_2$-sensing experiments, stock solutions of SOSG were prepared by dissolving 100 mg of SOSG in methanol (33 μL) to make a stock solution of approximately 5 mM. From the stock solution, 100 μL of 12 μM SOSG was added into 100 μL of D_2O solution containing a series of concentrations of ICG or AuNCs. The mixture of SOSG and ICG or AuNCs was vortex stirred before transferring to a sealed quartz cuvette with a volume of 300 μL. The resulting mixture was subjected to one-photon 808 nm CW laser excitation for 120 s. The mean power density on all samples was tuned to 23 mW cm^{-2}. Then the fluorescence enhancement of SOSG was recorded at 530 nm using an excitation light at 394 nm. In the case of NIR two-photon irradiation, a mode-locked femtosecond Ti:sapphire laser beam with an expanded diameter of 2 cm at 810 nm was used as the two-photon illumination source. The mean power density on the sample was tuned to 23 mW cm^{-2}, the same as that of the one-photon excitation source.

Quantitative Detection of •OH Generation. In a typical measurement, an MB solution in H_2O (20 μM, 100 μL) was first prepared and then mixed with 100 μL of 0.2 nM AuNCs. Then the mixture was vortex stirred before transferring to a sealed 300 μL quartz cuvette. The resulting mixture was subjected to laser treatment by an 808 nm CW laser as the NIR one-photon excitation source for 120 min. The mean power density on the sample was tuned to 23 mW cm^{-2}. Then absorption of MB at 664 nm was measured at constant time intervals (every 10 min). (Note: the UV−vis spectrum of the 0.1 nM AuNC dispersion was recorded as the corresponding baseline.) In the case of NIR two-photon irradiation, the sample was irradiated with two-photon light at a mean power density of 23 mW cm^{-2} to determine the production of •OH by 0.1 nM AuNCs or AuNCs-PEG, respectively.

Measurement of Intracellular ROS Production. CM-H_2DCFDA is deacetylated by intracellular esterase to form the more hydrophilic nonfluorescent reduced dye dichlorofluorescin, DCFH, which can be rapidly oxidized to form the highly fluorescent DCF in reaction with ROS. To evaluate intracellular ROS production *versus* two-photon irradiation power intensity, 5 × 10^4 cells mL^{-1} HeLa cells were grown in an eight-well glass-bottom Petri dish designed especially for confocal laser scanning microscopy (CLSM) observation, supplemented with culture medium to allow 90% confluence in 24 h. After 20 μL of 0.25 nM AuNCs-PEG was mixed with 180 μL of culture medium and incubated with the cells at 37 °C for 24 h, the cells were rinsed and supplemented with fresh culture medium. Then the cells were illuminated with a two-photon laser (810 nm, 14 or 0.40 pJ per pulse, 300 s) under an objective (60×, NA 1.35) with the continuous scanning mode, respectively. Soon afterward, the cells were incubated with 5 μM CM-H_2DCFDA at 37 °C for 30 min under darkness before being observed by CLSM. Fluorescence emission of CM-H_2DCFDA was collected mainly in the green channel through an emission filter at 500−550 nm when excited by a 488 nm Ar^+ laser. Cells in the absence of agent, without irradiation; without agent, under irradiation of a two-photon laser at 14 pJ per pulse for 300 s; in the presence of AuNCs-PEG, without irradiation; and in the presence of AuNCs-PEG and 250 μM ROS quenchers (histidine and mannitol), under irradiation of the laser at 14 pJ per pulse for 300 s were used as control groups. All fluorescent images were collected at the same setting. Fluorescence analysis was performed with Image software (FV10-ASW 3.1 Viewer).

Evaluation of Necrotic and Apoptotic Cells. Cell apoptosis and necrosis were determined using a standard apoptosis and necrosis kit. Assessment of cell viability was carried out by observing fluorescent cell staining: the annexin V specifically binds to exposed phosphatidylserines on apoptotic cell membranes in the presence of Ca^{2+}, while PI passes through the dead cell membrane and labeled DNA. In practice, after cells were cultured and delivered with AuNCs-PEG at the same experimental conditions as mentioned above in an eight-well glass-bottom Petri dish for 24 h, the cells were rinsed thoroughly and illuminated with the 810 nm two-photon laser (14 or 0.40 pJ per pulse, 300 s) under an objective (60×, NA 1.35) with the continuous scanning mode, respectively. Then cells were stained by annexin V-FITC/PI by following the manufacturer's protocol before observation by CLSM. Fluorescence emission of annexin V-FITC was collected mainly in the green channel through an emission filter at 500−545 nm when excited by a 488 nm laser, while that of PI was irradiated by a 559 nm laser and collected mainly in the red channel through an emission filter at 570−670 nm. Under irradiation of a laser at 14 or 0.40 pJ per pulse for 300 s, cells without any treatment or in the presence of AuNCs-PEG and 250 μM ROS quenchers (histidine and mannitol) were set as control groups. All fluorescent images were collected at the same setting. Fluorescence analysis was performed with Image software (FV10-ASW 3.1 Viewer). To observe late apoptotic HeLa cells, 24 and 48 h after irradiation of cells cocultured with AuNCs-PEG at 0.40 pJ per pulse, cells were stained by FITC-annexin V/PI and observed by CLSM.

Measurement of Mitochondrial Membrane Potential. We evaluated the mitochondrial membrane potential ($\Delta\Psi_m$) by mitochondrion-specific dye JC-1. At high mitochondrial membrane potential, the dye aggregates, yielding a red fluorescence emission. At low mitochondrial membrane potential, JC-1 is predominantly a monomer that yields green fluorescence. A decrease in the aggregate fluorescent count is indicative of mitochondrial membrane depolarization. In practice, after incubation with 0.025 nM AuNCs-PEG in an eight-well glass-bottom Petri dish for 24 h and irradiation by a laser at 0.40 pJ per pulse for 300 s, cells were rinsed and stained with freshly prepared JC-1 at 37 °C for 20 min in the dark by following the manufacturer's protocol. Then cells were thoroughly rinsed with cold buffer solution, and mitochondrial damage was determined by JC-1 aggregate/monomer fluorescence ratio through CLSM observation. JC-1 monomer was detected at the green emission channel (500−535 nm), and JC-1 aggregate was measured at the red emission channel (560−615 nm) with the same laser excitation of 488 nm. Under irradiation of a laser at 0.40 pJ per pulse, cells without AuNCs-PEG or irradiation and those in the presence of AuNCs-PEG and 250 μM ROS quenchers were used as control groups, respectively. All the fluorescent images were collected at the same setting.

Caspase-3/7 Activity Detection. NucView 488 caspase-3/7 substrate is a fluorescent probe that allows detection of caspase-3/7 activity in intact cells in real time. The substrate is designed by attaching a caspase-3/7 substrate peptide moiety to a nucleic acid dye. Once linked to the substrate peptide, the dye is unable to bind to DNA and remains nonfluorescent. The substrate crosses the plasma membrane to enter the cytoplasm, where it can be cleaved by caspase-3/7 to release the high-affinity DNA dye, which migrates to the cell nucleus to stain the nucleus with bright green fluorescence. After incubation with 0.025 nM AuNCs-PEG in an eight-well glass-bottom Petri dish for 24 h and irradiated by a laser at 0.40 pJ per pulse for 300 s, cells were rinsed and stained with freshly prepared NucView 488 caspase-3 substrate at 37 °C for 30 min in the dark by following the manufacturer's protocol. For end-point analysis, cells were rinsed with PBS and observed through CLSM using filters set for green fluorescence with the laser excitation at 488 nm. Cells without AuNCs-PEG or irradiation and those in the presence of AuNCs-PEG and 250 μM ROS quenchers (histidine and mannitol), under

irradiation of a laser at 0.40 pJ per pulse, were used as control groups, respectively. All the fluorescent images were collected at the same setting.

Conflict of Interest: The authors declare no competing financial interest.

Acknowledgment. We thank Prof. Jun-Jie Yin for helpful discussions. We acknowledge the financial support of this research by the National Key Basic Research Program of China (2013CB932703) and the Natural Science Foundation of China (21390410, 31271072, 31200751, 81201133, 81101743, and 31300827).

Supporting Information Available: The Supporting Information file contains ICP-MS measurements to determine the amount of essential component of the AuNCs; calculation of experimental and theoretical extinction coefficients of AuNCs; quantitative measurement of $^1O_2$ quantum yield; quantitative measurement of $^{\bullet}OH$ generation; cell culture, cell viability, and relevant cell assays. This material is available free of charge *via* the Internet at http://pubs.acs.org.

REFERENCES AND NOTES

1. Apel, K.; Hirt, H. Reactive Oxygen Species: Metabolism, Oxidative Stress, and Signal Transduction. *Annu. Rev. Plant Biol.* **2004**, *55*, 373–399.
2. Dolmans, D. E.; Fukumura, D.; Jain, R. K. Photodynamic Therapy for Cancer. *Nat. Rev. Cancer* **2003**, *3*, 380–387.
3. Phillips, D. Light Relief: Photochemistry and Medicine. *Photochem. Photobiol. Sci.* **2010**, *9*, 1589–1596.
4. Samia, A. C.; Chen, X.; Burda, C. Semiconductor Quantum Dots for Photodynamic Therapy. *J. Am. Chem. Soc.* **2003**, *125*, 15736–15737.
5. Yin, J. J.; Liu, J.; Ehrenshaft, M.; Roberts, J. E.; Fu, P. P.; Mason, R. P.; Zhao, B. Z. Phototoxicity of Nano Titanium Dioxides in HaCaT Keratinocytes—Generation of Reactive Oxygen Species and Cell Damage. *Toxicol. Appl. Pharmacol.* **2012**, *263*, 81–88.
6. Yamakoshi, Y.; Umezawa, N.; Ryu, A.; Arakane, K.; Miyata, N.; Goda, Y.; Masumizu, T.; Nagano, T. Active Oxygen Species Generated from Photoexcited Fullerene (C_{60}) as Potential Medicines: $O_2^{-\bullet}$ *versus* $^1O_2$. *J. Am. Chem. Soc.* **2003**, *125*, 12803–12809.
7. Murakami, T.; Nakatsuji, H.; Inada, M.; Matoba, Y.; Umeyama, T.; Tsujimoto, M.; Isoda, S.; Hashida, M.; Imahori, H. Photodynamic and Photothermal Effects of Semiconducting and Metallic-Enriched Single-Walled Carbon Nanotubes. *J. Am. Chem. Soc.* **2012**, *134*, 17862–17865.
8. Joshi, A.; Punyani, S.; Bale, S. S.; Yang, H.; Borca-Tasciuc, T.; Kane, R. S. Nanotube-Assisted Protein Deactivation. *Nat. Nanotechnol.* **2007**, *3*, 41–45.
9. Vankayala, R.; Sagadevan, A.; Vijayaraghavan, P.; Kuo, C. L.; Hwang, K. C. Metal Nanoparticles Sensitize the Formation of Singlet Oxygen. *Angew. Chem., Int. Ed.* **2011**, *50*, 10640–10644.
10. Pasparakis, G. Light-Induced Generation of Singlet Oxygen by Naked Gold Nanoparticles and Its Implications to Cancer Cell Phototherapy. *Small* **2013**, *9*, 4130–4134.
11. Vankayala, R.; Kuo, C.; Sagadevan, A.; Chen, P.; Chiang, C.; Hwang, K. C. Morphology Dependent Photosensitization and Formation of Singlet Oxygen ($^1\Delta g$) by Gold and Silver Nanoparticles and Its Application in Cancer Treatment. *J. Mater. Chem. B* **2013**, *1*, 4379–4387.
12. Zhao, T.; Shen, X.; Li, L.; Guan, Z.; Gao, N.; Yuan, P.; Yao, S. Q.; Xu, Q. H.; Xu, G. Q. Gold Nanorods as Dual Photo-Sensitizing and Imaging Agents for Two-Photon Photodynamic Therapy. *Nanoscale* **2012**, *4*, 7712–7719.
13. Vankayala, R.; Huang, Y. K.; Kalluru, P.; Chiang, C. S.; Hwang, K. C. First Demonstration of Gold Nanorods-Mediated Photodynamic Therapeutic Destruction of Tumors *via* Near Infra-Red Light Activation. *Small* **2014**, *10*, 1612–1622.
14. Hohlfeld, J.; Wellershoff, S. S.; Güdde, J.; Conrad, U.; Jähnke, V.; Matthias, E. Electron and Lattice Dynamics Following Optical Excitation of Metals. *Chem. Phys.* **2000**, *251*, 237–258.
15. Aruda, K. O.; Tagliazucchi, M.; Sweeney, C. M.; Hannah, D. C.; Schatz, G. C.; Weiss, E. A. Identification of Parameters through Which Surface Chemistry Determines the Lifetimes of Hot Electrons in Small Au Nanoparticles. *Proc. Natl. Acad. Sci. U.S.A.* **2013**, *110*, 4212–4217.
16. Qin, Z.; Bischof, J. C. Thermophysical and Biological Responses of Gold Nanoparticle Laser Heating. *Chem. Soc. Rev.* **2012**, *41*, 1191–1217.
17. Huang, X. H.; El-Sayed, M. A. Plasmonic Photo-Thermal Therapy (PPTT). *Alex. J. Med.* **2011**, *47*, 1–9.
18. Krpetić, Z.; Nativo, P.; Sée, V.; Prior, I. A.; Brust, M.; Volk, M. Inflicting Controlled Nonthermal Damage to Subcellular Structures by Laser-Activated Gold Nanoparticles. *Nano Lett.* **2010**, *10*, 4549–4554.
19. Skrabalak, S. E.; Au, L.; Li, X. D.; Xia, Y. N. Facile Synthesis of Ag Nanocubes and Au Nanocages. *Nat. Protoc.* **2007**, *2*, 2182–2190.
20. Long, R.; Mao, K. K.; Ye, X. D.; Yan, W. S.; Huang, Y. B.; Wang, J. Y.; Fu, Y.; Wang, X. S.; Wu, X. J.; Xie, Y.; *et al*. Surface Facet of Palladium Nanocrystals: a Key Parameter to the Activation of Molecular Oxygen for Organic Catalysis and Cancer Treatment. *J. Am. Chem. Soc.* **2013**, *135*, 3200–3207.
21. Yu, C. L.; Chen, S.; Zhang, M. H.; Shen, T. Spectroscopic Studies and Photodynamic Actions of Hypocrellin B in Liposomes. *Photochem. Photobiol.* **2001**, *73*, 482–488.
22. Inbaraj, J. J.; Bilski, P.; Chignell, C. F. Photophysical and Photochemical Studies of 2-Phenylbenzimidazole and UVB Sunscreen 2-Phenylbenzimidazole-5-Sulfonic Acid. *Photochem. Photobiol.* **2002**, *75*, 107–116.
23. Kato, M.; Cardona, T.; Rutherford, A. W.; Reisner, E. Photoelectrochemical Water Oxidation with Photosystem II Integrated in a Mesoporous Indium-Tin Oxide Electrode. *J. Am. Chem. Soc.* **2012**, *134*, 8332–8335.
24. Christopher, P.; Xin, H. L.; Marimuthu, A.; Linic, S. Singular Characteristics and Unique Chemical Bond Activation Mechanisms of Photocatalytic Reactions on Plasmonic Nanostructures. *Nat. Mater.* **2012**, *11*, 1044–1050.
25. Mukherjee, S.; Libisch, F.; Large, N.; Neumann, O.; Brown, L. V.; Cheng, J.; Lassiter, J. B.; Carter, E. A.; Nordlander, P.; Halas, N. J. Hot Electrons Do the Impossible: Plasmon-Induced Dissociation of H_2 on Au. *Nano Lett.* **2012**, *13*, 240–247.
26. Lin, H. Y.; Shen, Y.; Chen, D. F.; Lin, L. S.; Wilson, B. C.; Li, B. H.; Xie, S. S. Feasibility Study on Quantitative Measurements of Singlet Oxygen Generation Using Singlet Oxygen Sensor Green. *J. Fluoresc.* **2013**, *23*, 41–47.
27. Gomes, A. J.; Lunardi, L. O.; Marchetti, J. M.; Lunardi, C. N.; Tedesco, A. C. Indocyanine Green Nanoparticles Useful for Photomedicine. *Photomed. Laser Surg.* **2006**, *24*, 514–521.
28. Hu, M.; Petrova, H.; Chen, J. Y.; McLellan, J. M.; Siekkinen, A. R.; Marquez, M.; Li, X. D.; Xia, Y. N.; Hartland, G. V. Ultrafast Laser Studies of the Photothermal Properties of Gold Nanocages. *J. Phys. Chem. B* **2006**, *110*, 1520–1524.
29. Lee, Y. K.; Jung, C. H.; Park, J.; Seo, H.; Somorjai, G. A.; Park, J. Y. Surface Plasmon-Driven Hot Electron Flow Probed with Metal-Semiconductor Nanodiodes. *Nano Lett.* **2011**, *11*, 4251–4255.
30. Romanov, A. N.; Bykhovskii, M. Y.; Rufov, Y. N.; Korchak, V. N. Thermal Generation of Singlet Oxygen on Zeolite ZSM-5. *Kinet. Catal.* **2000**, *41*, 782–786.
31. Chen, J. Y.; Saeki, F.; Wiley, B. J.; Cang, H.; Cobb, M. J.; Li, Z. Y.; Au, L.; Zhang, H.; Kimmey, M. B.; Li, X. D.; *et al*. Gold Nanocages: Bioconjugation and Their Potential Use As Optical Imaging Contrast Agents. *Nano Lett.* **2005**, *5*, 473–477.
32. Satoh, A. Y.; Trosko, J. E.; Masten, S. J. Methylene Blue Dye Test for Rapid Qualitative Detection of Hydroxyl Radicals Formed in a Fenton's Reaction Aqueous Solution. *Environ. Sci. Technol.* **2007**, *41*, 2881–2887.
33. Velusamy, M.; Shen, J. Y.; Lin, J. T.; Lin, Y. C.; Hsieh, C. C.; Lai, C. H.; Lai, C. W.; Ho, M. L.; Chen, Y. C.; Chou, P. T. A New Series of Quadrupolar Type Two-Photon Absorption Chromophores Bearing 11, 12-Dibutoxydibenzo [a, c]-Phenazine Bridged Amines; Their Applications in Two-Photon Fluorescence Imaging and Two-Photon Photodynamic Therapy. *Adv. Funct. Mater.* **2009**, *19*, 2388–2397.

34. Gao, L.; Fei, J. B.; Zhao, J.; Li, H.; Cui, Y.; Li, J. B. Hypocrellin-Loaded Gold Nanocages with High Two-Photon Efficiency for Photothermal/Photodynamic Cancer Therapy *in Vitro*. *ACS Nano* **2012**, *6*, 8030–8040.
35. Tong, L.; Zhao, Y.; Huff, T. B.; Hansen, M. N.; Wei, A.; Cheng, J. X. Gold Nanorods Mediate Tumor Cell Death by Compromising Membrane Integrity. *Adv. Mater.* **2007**, *19*, 3136–3141.
36. Qin, Z. P.; Bischof, J. C. Thermophysical and Biological Responses of Gold Nanoparticle Laser Heating. *Chem. Soc. Rev.* **2012**, *41*, 1191–1217.
37. Agostinis, P.; Buytaert, E.; Breyssens, H.; Hendrickx, N. Regulatory Pathways in Photodynamic Therapy Induced Apoptosis. *Photochem. Photobiol. Sci.* **2004**, *3*, 721–729.
38. Wang, L. M.; Liu, Y.; Li, W.; Jiang, X. M.; Ji, Y. L.; Wu, X. C.; Xu, L. G.; Qiu, Y.; Zhao, K.; Wei, T. T.; *et al*. Selective Targeting of Gold Nanorods at the Mitochondria of Cancer Cells: Implications for Cancer Therapy. *Nano Lett.* **2011**, *11*, 772–780.
39. Robles-Escajeda, E.; Lerma, D.; Nyakeriga, A. M.; Ross, J. A.; Kirken, R. A.; Aguilera, R. J.; Varela-Ramirez, A. Searching in Mother Nature for Anti-Cancer Activity: Anti-Proliferative and Pro-Apoptotic Effect Elicited by Green Barley on Leukemia/Lymphoma Cells. *PloS One* **2013**, *8*, e73508.
40. Fink, S. L.; Cookson, B. T. Apoptosis, Pyroptosis, and Necrosis: Mechanistic Description of Dead and Dying Eukaryotic Cells. *Infect. Immun.* **2005**, *73*, 1907–1916.
41. Vanden Berghe, T.; Kalai, M.; Denecker, G.; Meeus, A.; Saelens, X.; Vandenabeele, P. Necrosis Is Associated with IL-6 Production But Apoptosis Is Not. *Cell. Signal.* **2006**, *18*, 328–335.
42. Bear, A. S.; Kennedy, L. C.; Young, J. K.; Perna, S. K.; Almeida, J. P. M.; Lin, A. Y.; Eckels, P. C.; Drezek, R. A.; Foster, A. E. Elimination of Metastatic Melanoma Using Gold Nanoshell-Enabled Photothermal Therapy and Adoptive T Cell Transfer. *PloS One* **2013**, *8*, e69073.